JOURNAL OF SPACECRAFT AND ROCKETS
Vol. 54, No. 2, March–April 2017

Dynamic Beam Solutions for Real-Time Simulation and Control Development of Flexible Rockets

Weihua Su* and Cecilia K. King†
University of Alabama, Tuscaloosa, Alabama 35487
Scott R. Clark‡ and Edwin D. Griffin§
A.I. Solutions, Inc., Cape Canaveral, Florida 32920
and
Jeffrey D. Suhey¶ and Michael G. Wolf**
NASA Kennedy Space Center, Kennedy Space Center, Florida 32899

DOI: 10.2514/1.A33543

In this study, flexible rockets are structurally represented by linear beams. Both direct and indirect solutions of beam dynamic equations are sought to facilitate real-time simulation and control development for flexible rockets. The direct solution is obtained by numerically integrating the beam structural dynamic equation using an explicit Newmark-based scheme, which allows for stable and fast transient solutions to the dynamics of flexile rockets. Furthermore, in real-time operation, the bending strain of the beam is measured by fiber-optical sensors at discrete locations along the span, whereas both the angular velocity and translational acceleration are measured at a single point by an inertial measurement unit. Another aspect in this paper is finding the analytical and numerical solutions of the beam dynamics based on limited measurement data to facilitate the real-time control development. Numerical studies demonstrate the accuracy of these real-time solutions of the beam dynamics. Such analytical and numerical solutions, when integrated with data processing and control algorithms and mechanisms, have the potential to increase launch availability by processing flight data into the flexible launch vehicle's control system.

Nomenclature

A	=	coefficient matrix using Legendre polynomials to approximate finite element model modes
a_B	=	beam base excitation acceleration, m/s^2
a_z	=	nodal translational acceleration in lateral direction, m/s^2
b	=	beam cross-section thickness, m
C	=	beam damping matrix of finite element model
E	=	beam Young's modulus, Pa
EI_y	=	beam bending rigidity, N · m^2
F	=	beam load vector of finite element model
h	=	beam cross-section width, m
K	=	beam stiffness matrix of finite element model
L	=	beam span, m
M	=	beam mass matrix of finite element model
m	=	beam mass per unit length, kg/m
P_n	=	shifted Legendre polynomials
p	=	lateral distributed load of beam, N/m
s	=	inertial measurement unit location, m
t	=	time, s
u	=	beam nodal translation and rotation of finite element model
w	=	nodal lateral displacement due to beam bending, m
x	=	spanwise position along beam, m
z_0	=	distance from beam reference line to locations of fiber-optic sensors, m
α	=	damping coefficient
α_1, α_2	=	tuning parameters in numerical integration
ε_x	=	tensile/compressive strain due to bending
η	=	magnitude of modes
θ	=	nodal rotation due to beam bending, rad
κ_y	=	bending curvature, 1/m
ξ	=	general coordinate
ρ	=	beam material density, kg/m^3
Φ	=	beam bending mode shape matrix
φ	=	individual beam bending mode shape vector
ω	=	beam bending natural frequencies, Hz
ω_y	=	nodal angular velocity about y direction, rad/s

Presented as Paper 2016-1954 at the 57th AIAA/ASCE/AHS/ASC Structures, Structural Dynamics, and Materials Conference, San Diego, CA, 4–8 January 2016; received 23 December 2015; revision received 2 October 2016; accepted for publication 3 October 2016; published online 19 January 2017.

*Assistant Professor, Department of Aerospace Engineering and Mechanics; suw@eng.ua.edu. Senior Member AIAA.
†Graduate Research Assistant, Department of Aerospace Engineering and Mechanics; ckking1@crimson.ua.edu. Student Member AIAA.
‡Project Manager; scott.r.clark@nasa.gov.
§Research Scientist; edwin.d.griffin@nasa.gov.
¶Flight Structures Analyst; jeffrey.d.suhey@nasa.gov.
**Research Scientist; michael.wolf@nasa.gov.

I. Introduction

THE study of flight dynamics of rockets involves the modeling of the airframe, the propulsion, and the aerodynamic loads acting on the airframe. Traditionally, rockets are considered as rigid bodies in their flight dynamic modeling [1–5]. The six-degree-of-freedom dynamic equations describing the trajectory of the rigid body are usually established by applying Newton's second law or Lagrange's equation [6]. Another study [7] modeled a rocket as an assemblage of multiple-hinged rigid bodies. Such modeling allows for consideration of the transverse vibration of the rocket and its aeroelastic behavior due to the interaction with the aerodynamic loads. Future rockets are likely to be larger, with more capacity to launch heavier payloads. At the same time, the structural weight fraction of the new rocket airframes will need to be reduced to accommodate more payloads and fuel. Consequently, this will result in much more flexible rocket designs. For flexible rockets, their transverse bending vibration may be easily excited by lateral aerodynamic loads, which may significantly impact the attitude control system's stability if the control system is designed based on a rigid-body model [8]. To take into account airframe flexibility, different approaches have been applied in the modeling of rocket flight dynamics, such as the linear beam approach [9] and flexible multibody approach [10]. Moreover, adaptive control algorithms have been developed [8], where the rocket flight dynamic response was also modeled using a linear beam

theory. In fact, due to the interactions between flexible structures and the aerodynamic loads, aeroelastic characteristics and behaviors of flexible launch vehicles need to be properly modeled in numerical simulations. An early study by Crimi [11] identified the impacts of static and dynamic aeroelastic behaviors of flexible tactical weapons using a linear beam model. In [12,13], Chae and Hodges modeled the flight dynamics of flexible missiles using a mixed-form geometrically nonlinear beam formulation, coupled with the combined viscous crossflow theory [14] and the potential flow slender-body theory [15]. They studied the flight stability of such vehicles and the impact of the thrust force on their flight stability. In a more recent study, Bartels et al. [16] studied aeroelastic characteristics and stability of the Ares I launch vehicle by coupling the Reynolds-averaged Navier–Stokes computational fluid dynamics (CFD) solver FUN3D with a linear modal-based bean model. They suggested that a correct aeroelastic coupling model was needed to predict dynamic flexible vehicle behavior, especially in the transonic flight region. The work also provided a good summary of different approaches for modeling the aeroelasticity of flexible launch vehicles.

However, during an individual launch, the excitation and loading on the flexible rocket, especially the instantaneous lateral aerodynamic loads acting on the flexible body, may not be available from measurements. Atmospheric wind gust is random and difficult to predict in an individual launch. Measurements from onboard sensors may be used to directly track the dynamics of the vehicle and further control it. For example, fiber-optic sensors (FOSs) can be used to measure the strain of a flexible body [17]. Recently, FOS systems have been applied in aircraft and launch vehicle development at the NASA Armstrong Flight Research Center [18] and Kennedy Space Center [19]. During the launch, FOS systems are able to observe the bending/torsion deformation of the airframe. It is also of interest to potentially use the measured structural deformation from the FOS system to control the bending/torsion vibration of the flexible rocket, with appropriately designed control algorithms. Additionally, both the angular velocity and translational acceleration can be measured at a single point by the inertial measurement unit (IMU) to provide some dynamic characteristics of the rocket. Figure 1 illustrates the distribution of the sensors and measurements along a beam representation of a flexible rocket. Such information will be the only input to an indirect solution (compared to the traditional solutions of launch vehicles with thrust and aerodynamics loads predicted from corresponding numerical models) of the beam dynamics. The indirect solution needs to provide the beam bending dynamics, including the angular velocity and translational acceleration along the beam, for further control development for flexible rockets. An operational constraint that must be considered in this solution is the sampling frequencies of the sensors and the onboard computer. Basically, the sampling frequencies of FOSs and IMUs are 1000 and 100 Hz, respectively, whereas the onboard autopilot system operates at a lower frequency of 50 Hz. Theoretically, the beam bending dynamics should be computed within, at most, 0.02 s based on those sampling frequencies. An even faster solution will be required to allow for the response of the control system and data processing. From this point of view, a very fast indirect beam dynamics solution is needed to support the real-time control operation of flexible rockets, taking advantage of the onboard FOS and IMU measurements. The functional blocks of this solution are illustrated in the top path of Fig. 2, with the shaded block to be implemented in the real-time sense to satisfy the operation requirement.

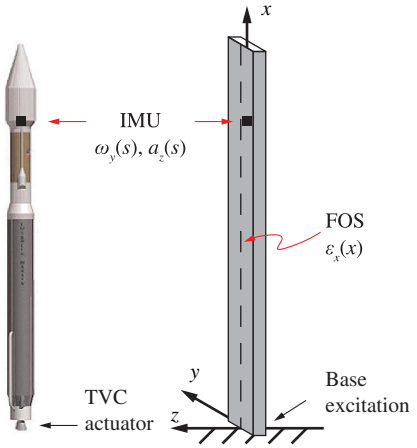

Fig. 1 Beam representation of flexible rocket and the distribution of sensor measurements (TVC, thrust vector control; comp., component; Norm., normalized).

This paper basically focuses on the dynamic beam solutions. A control algorithm, based on a testing beam article, has been implemented using MATLAB/Simulink [20], where the indirect solution from the current study is integrated. However, further development of control algorithms that are suitable for practical applications in full-size flexible rockets is still ongoing. In this process, it is desired to have a numerical tool to simulate the real-time behavior of flexible rockets, and thus to facilitate benchmarking different control algorithms for the altitude control of the rockets. Therefore, the current work also aims at developing a real-time dynamic simulation for flexible rockets. This is shown as the bottom path in Fig. 2, where a direct solution of the real-time beam dynamics is sought. The linear Euler–Bernoulli beam theory will be applied to model flexible rockets. In this development, the first need is a numerical integration scheme for the beam dynamic equations that is stable and fast enough to allow for the real-time simulations. Implicit schemes (e.g., [21]) may provide numerically stable transient simulation results of dynamic systems. However, the subiterations inherently associated to these schemes prohibit them from providing the real-time simulation capability. Therefore, an explicit integration scheme will be the choice for the real-time simulation, provided that it maintains the numerical stability of results with relatively larger time steps, which is also critical to ensure the real-time simulation capability. The explicit Newmark-based scheme developed by Chen and Ricles [22] is used in the current study.

Both indirect and direct dynamic beam solutions are developed in this paper, as highlighted in Fig. 2. The indirect solution intends to facilitate the real-time control operation using the FOS and IMU measurement data during the launch of a flexible rocket, whereas the direct solution can be used to benchmark the rocket attitude control algorithms. Particularly, in this study, due to the lack of real sensor measurement data during the launch, the direct solution of the beam dynamics can be used as the input for the indirect solution, as the dashed line shows in Fig. 2. Because the bending mode has a strong contribution to the attitude control of flexible rockets, only the one-dimensional bending of the beam is considered in this study, with a base motion to excite the beam. The aeroelastic effect is not involved in the direct solution. Additionally, it has been shown that longitudinal forces (thrusts) may impact the bending behavior of a flexible launch vehicle [12,13,23]. This effect is not involved in the current study, but the solution approaches developed can be adapted to include multiaxial loading conditions. The analytical solution and the numerical implementation of this work will have the potential to increase launch availability by processing real-time flight data (including the deformation and kinematics) into the flexible launch vehicle's control system.

II. Theoretical Formulation

Flexible rockets are modeled as linear beams by taking advantage of their geometry. A specific constraint to the current study is that the beam dynamic responses should be solved at a real-time rate. Therefore, the solutions of the beam bending equations of motion need some special treatment.

A. Euler–Bernoulli Beam Equation of Motion

In the current study, a flexible rocket is modeled using Euler–Bernoulli beam theory. As shown in Fig. 3, the flexible rocket is treated as a cantilever beam in a moving frame (xyz) that is fixed at the root. The aerodynamic loads of the rocket are not included in this study. However, the rocket's lateral bending vibration can be excited by a base acceleration $a_B(t)$. So, the lateral distributed force $p(x, t)$ along the beam is derived from the base acceleration:

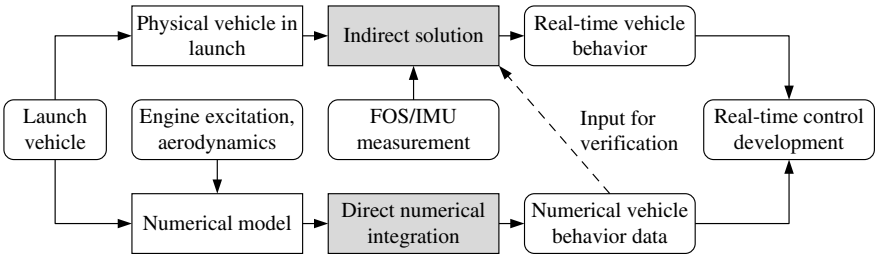

Fig. 2 Block diagram of the real-time solutions for flexible launch vehicles.

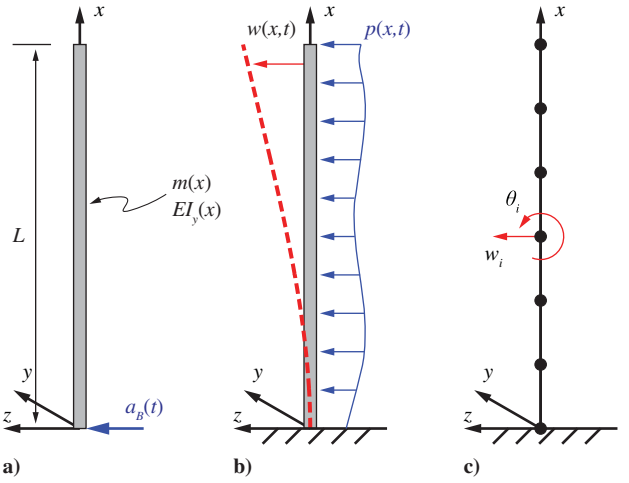

Fig. 3 Description of a continuous beam and its finite element discretization.

$$p(x,t) = -m(x)a_B(t) \tag{1}$$

where $m(x)$ is the mass per unit length of the beam. Only the flatwise bending about the y axis is considered. The equation of motion for the beam is given as

$$(EI_y(x)w''(x,t))'' + m(x)\ddot{w}(x,t) = p(x,t) \tag{2}$$

where $w(x,t)$ is the beam's lateral displacement relative to the moving frame xyz, and $EI_y(x)$ is its bending rigidity about the y axis. The cross section of the beam model is obtained from a testing beam article with a solid cross section. The warping of the cross section is not considered. Note that $(\cdot\cdot)$ denotes the second time derivative, whereas $()'$ and $()''$ denote spatial partial derivatives of the corresponding variable. The cantilever boundary condition should be satisfied. In general, the inertial and rigidity properties of a representative beam model derived from a rocket are not uniform along its span and several rigid-body masses (e.g., the boosters and payloads) may be attached to the rocket. Therefore, the analytical solution to Eq. (2) is usually not available for a rocket bending problem and the finite element approach is used to solve the governing equation. The finite element discretization of Eq. (2) using two-node beam elements results in the following second-order differential equation:

$$[M]\{\ddot{u}\} + [C]\{\dot{u}\} + [K]\{u\} = \{F\} \tag{3}$$

Each beam node has a translational w and a rotational θ degree of freedom, i.e.,

$$\{u_i\} = \begin{Bmatrix} w_i \\ \theta_i \end{Bmatrix} = \begin{Bmatrix} w_i \\ w_i' \end{Bmatrix} \tag{4}$$

where the rotational degree is the spatial derivative of the translational degree, according to Euler–Bernoulli beam theory. The inertia $[M]$ and stiffness $[K]$ matrices are obtained from the assemblage of the elemental matrices. In the initial finite element model, a stiffness-proportional damping is assumed:

$$[C] = \alpha[K] \tag{5}$$

In a following modal-based transient solution of Eq. (3), the stiffness-proportional damping is converted to the modal damping using the modal transformation. The finite element model is compatible to both uniform and nonuniform beams. Concentrated inertias, if present, can be attached to the corresponding nodes in the finite element model.

B. Kinematics

According to the kinematics of Euler–Bernoulli beams, the tensile strain due to the beam bending is related to the nodal displacement:

$$\varepsilon_x(x,t) = -z_0 w''(x,t) \tag{6}$$

where z_0 is the distance from the beam neutral axis (centerline for this study) to locations of the FOS, where the strains are measured, which is usually the surface of the beam. Additionally, the angular velocity and translational acceleration are

$$a_z(x,t) = \ddot{w}(x,t) \quad \omega_y(x,t) = \dot{\theta}_y(x,t) = \dot{w}'(x,t) \tag{7}$$

C. Normal Modes and Approximation Using Continuous Functions

The nodal displacement of the beam is considered as a linear combination of the normal modes, given as

$$\{u(t)\} = \sum_{j=1}^{N} \{\varphi_j\}\eta_j(t) = [\Phi]\{\eta(t)\} \tag{8}$$

where φ_j are the normal modes of the beam, obtained from the eigenvalue solution of Eq. (3); and η_j are the magnitudes of the corresponding modes varying in time. The nodal degrees in Eq. (8) can be reorganized, such that

$$\{w(t)\} = [\Phi_w]\{\eta(t)\} \quad \{\theta(t)\} = [\Phi_\theta]\{\eta(t)\} \tag{9}$$

where $[\Phi_w]$ and $[\Phi_\theta]$ are both subsets of $[\Phi]$. Note that the nodal rotation is essentially a spatial derivative of the nodal translation, according to Euler–Bernoulli beam theory.

However, the normal mode matrix $[\Phi]$ and its subsets derived from the eigenvalue solution of Eq. (3) are discrete, represented by the eigendisplacement and rotation at each node of the finite element model. There are no analytical functions of the mode shapes that are directly available from the eigenvalue solution of Eq. (3). To estimate the spatial derivatives of the mode shapes in Eqs. (6) and (7) at any spanwise position along the beam, the discrete mode shapes can be approximated by using some analytical functions. In the current study, this is done by using the shifted Legendre polynomials [24], which are a set of complete and orthogonal polynomials defined in the domain of [0,1]. The general equations for the shifted Legendre polynomials are given as

$$P_0(x) = 1, \qquad P_1(x) = 2x - 1,$$
$$P_{i+1}(x) = \frac{(2i+1)(2x-1)P_i(x) - iP_{i-1}(x)}{i+1} \tag{10}$$

The first few shifted Legendre polynomials are plotted in Fig. 4.

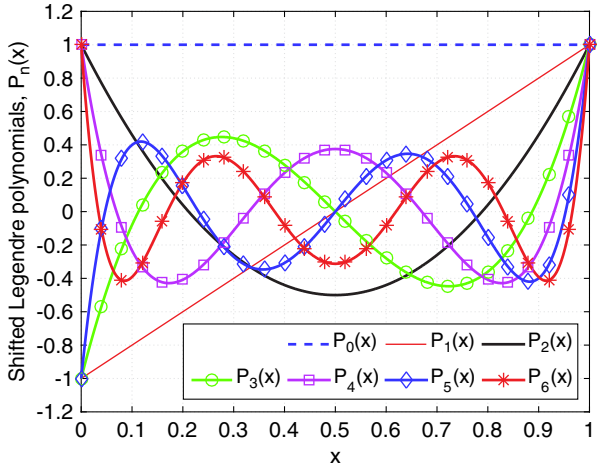

Fig. 4 First seven shifted Legendre polynomials.

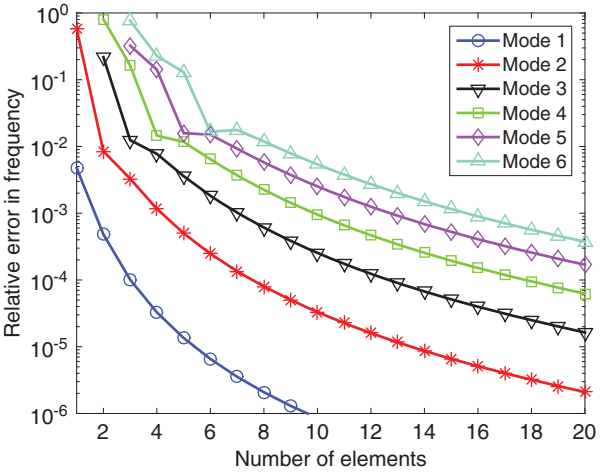

Fig. 5 Relative errors of natural frequencies from the finite element solutions, compared with the analytical solutions.

Linear combinations of Legendre polynomials can be used to fit any functions. Any discrete mode shape φ_j can be fitted by linear combinations of the first $m+1$ shifted Legendre polynomials:

$$\{\varphi_{jw}\} = \sum_{i=0}^{\infty} a_{ij}\{P_i\} \approx a_{0j}\{P_0\} + a_{1j}\{P_1\} + \cdots + a_{mj}\{P_m\} \quad (11)$$

where φ_{jw} consists only of the translational components of the jth mode. P_i are the shifted Legendre polynomials evaluated at the nodal coordinates of the finite element model. The coefficients a_{ij} are yet to be determined. This approximation can be done for all modes (translational components only), resulting in

$$\begin{aligned}[\Phi_w] &= [\,\varphi_{1w} \quad \varphi_{2w} \quad \cdots \quad \varphi_{nw}\,] \\ &= [\,P_0 \quad P_1 \quad P_2 \quad \cdots \quad P_m\,]\begin{bmatrix} a_{01} & a_{02} & \cdots & a_{0n} \\ a_{11} & a_{12} & \cdots & a_{1n} \\ a_{21} & a_{22} & \cdots & a_{2n} \\ \vdots & \vdots & \cdots & \vdots \\ a_{m1} & a_{m2} & \cdots & a_{mn} \end{bmatrix} \\ &= [P][A] \end{aligned} \quad (12)$$

Table 1 Properties of a uniform beam

Property	Value
Span L, m	1.575
Cross-section thickness b, m	4.826×10^{-3}
Cross-section width h, m	2.543×10^{-2}
Material density ρ, kg/m^3	2.666×10^{3}
Young's modulus E, Pa	6.350×10^{10}

Table 2 Natural frequencies (in hertz) of the uniform cantilever beam

	Finite element solution				
Mode	5 elements	10 elements	14 elements	20 elements	Analytical solution
1	1.5343	1.5343	1.5343	1.5343	1.5343
2	9.6201	9.6156	9.6154	9.6153	9.6153
3	27.020	26.930	26.925	26.924	26.923
4	53.377	52.809	52.772	52.762	52.759
5	88.593	87.434	87.274	87.229	87.214
6	147.18	130.99	130.48	130.33	130.28
7	215.25	183.78	182.49	182.10	181.96
8	312.16	246.21	243.46	242.57	242.26

Therefore, the coefficient matrix $[A]$ is solved by

$$[A] = [P]^{-1}[\Phi_w] \quad (13)$$

with given mode shapes $[\Phi_w]$. The dimension of $[P]$ is determined by the dimension of the initial finite element model and the number of the shifted Legendre polynomials used in the approximation. Thus, it is generally invertible. Instead, the Moore–Penrose pseudoinverse of $[P]$ is used. Once $[A]$ is determined, the spatial derivatives of the beam spanwise deformation are obtained by differentiating the continuous polynomials $P(x)$, according to Euler–Bernoulli beam theory, yielding

$$\begin{aligned} \{w(x,t)\} &= [P(x)][A]\{\eta(t)\} \\ \{w'(x,t)\} &= \{\theta_y(x,t)\} = [P'(x)][A]\{\eta(t)\} \\ \{w''(x,t)\} &= \{-\kappa_y(x,t)\} = [P''(x)][A]\{\eta(t)\} \end{aligned} \quad (14)$$

From Eqs. (6), (7), and (14), one can find the strain, angular velocity, and translational acceleration at any spanwise locations along the beam:

$$\begin{aligned} \varepsilon_x(x,t) &= -z_0[P''(x)][A]\{\eta(t)\} \\ \omega_y(x,t) &= [P'(x)][A]\{\dot{\eta}(t)\} \\ a_z(x,t) &= [P(x)][A]\{\ddot{\eta}(t)\} \end{aligned} \quad (15)$$

The matrix $[A]$ is only calculated once for a given beam, as long as the finite element model and the involved Legendre polynomials are both fixed. $[P][A]$ is an approximation to the mode shapes of the beam, and $[A]$ does not change with the applied loads. If a different beam theory with independent nodal translations and rotations (e.g., the Timoshenko beam) is used to create the finite element model, the approximation of the translational and rotational mode shapes should be completed individually.

D. Modal Transformation of Equation of Motion

To reduce the number of degrees of freedom and save time in real-time transient simulations, a modal transformation is performed with Eq. (3). To be consistent with the transformation of mode shapes into the combinations of the shifted Legendre polynomials, complete mode shapes from the finite element equation (consisting of both nodal translations and rotations) are represented as

$$[\Phi] = [\bar{P}][A] \quad (16)$$

where each column of $[P^-]$ is formed by alternate components from $[P]$ and $[P']$. Therefore, the finite element solution is represented by the shifted Legendre polynomials as

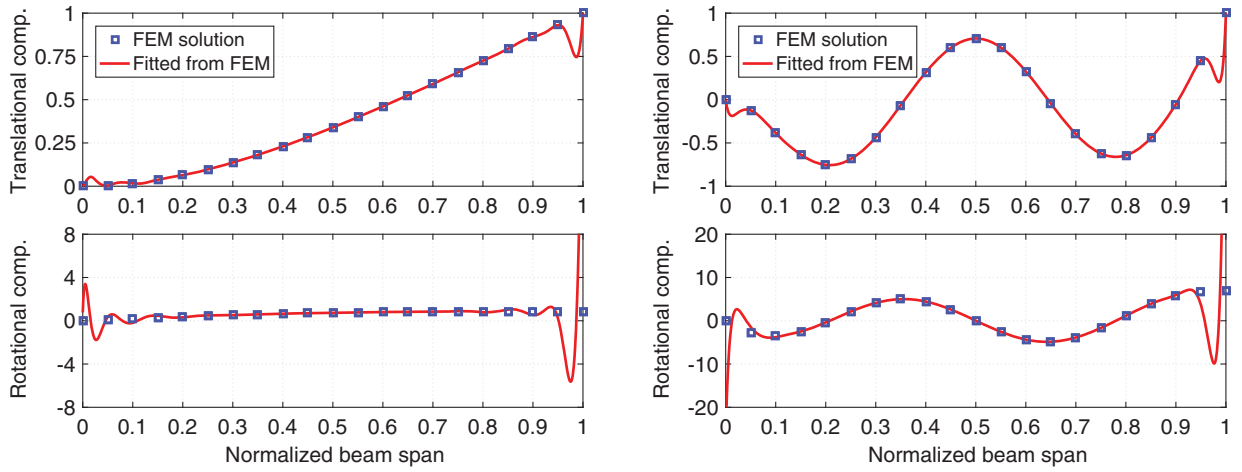

a) First bending mode b) Fourth bending mode

Fig. 6 Improperly fitted mode shapes using excessive Legendre polynomials.

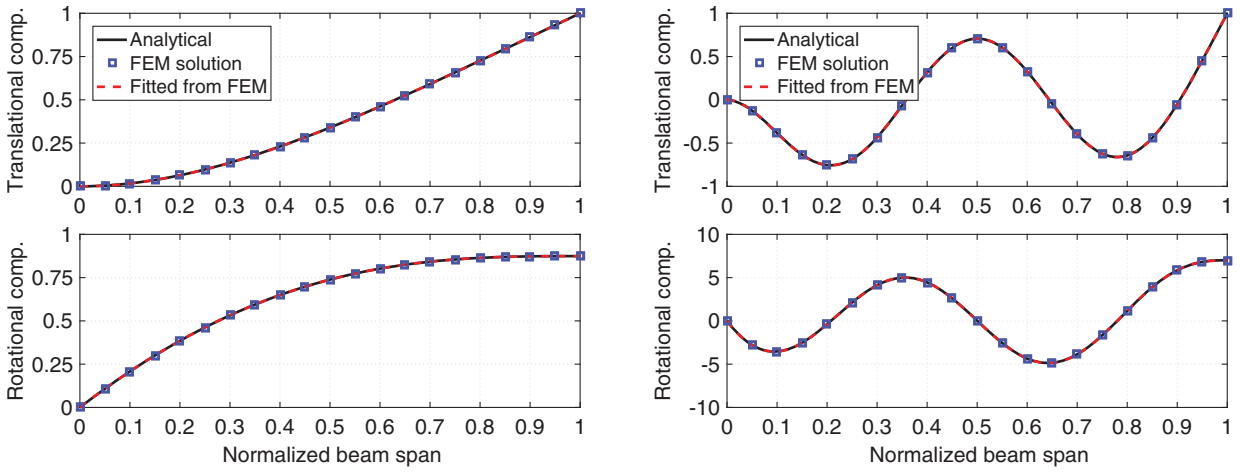

a) First bending mode b) Fourth bending mode

Fig. 7 Cantilever beam bending mode shapes from analytical and finite element (20 elements) solutions and the fitted continuous shape (using 20 shifted Legendre polynomials).

$$\{u(t)\} = [\Phi]\{\eta(t)\} = [\bar{P}][A]\{\eta(t)\} \tag{17}$$

Substituting Eq. (17) into Eq. (3) and premultiplying $[[A]^T[P^-]^T$ on both sides of the equation yields the modal-based equation of motion:

$$[\bar{M}]\{\ddot{\eta}\} + [\bar{C}]\{\dot{\eta}\} + [\bar{K}]\{\eta\} = \{\bar{F}\} \tag{18}$$

where

$$\begin{aligned}[\bar{M}] &= [A]^T[\bar{P}]^T[M][\bar{P}][A]\\ [\bar{C}] &= [A]^T[\bar{P}]^T[C][\bar{P}][A]\\ [\bar{K}] &= [A]^T[\bar{P}]^T[K][\bar{P}][A]\\ \{\bar{F}\} &= [A]^T[\bar{P}]^T\{F\}\end{aligned} \tag{19}$$

The time-domain transient analysis of the flexible rocket can be done with either Eq. (3) or Eq. (18). However, Eq. (18) usually involves significantly fewer degrees of freedom than Eq. (3).

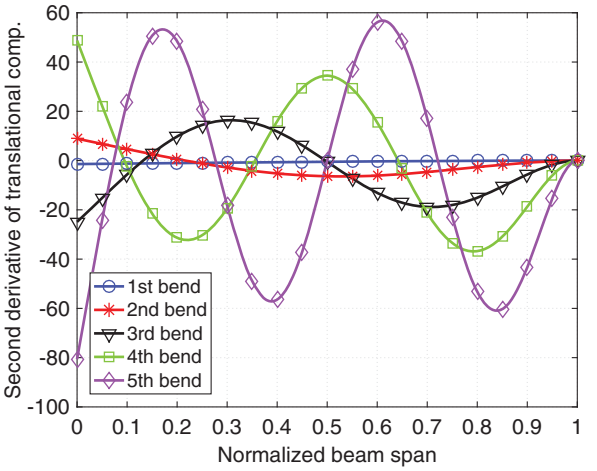

Fig. 8 Second derivatives of the first five modes.

E. Direct Solution

The numerical integration of the equation of motion [Eq. (3) or Eq. (18)] is needed to obtain the transient response of the flexible rocket. An explicit numerical integration scheme is selected over implicit approaches to provide fast solutions of the beam dynamic response, facilitating the real-time simulations. The explicit integration scheme developed by Chen and Ricles [22,25], which has been proved to be unconditionally stable [25], is implemented here. This allows for the use of relatively larger time steps in transient solutions while maintaining numerical stability. For a second-order equation of motion [Eq. (3) or (18)], the "velocity" and "displacement" at each time step are determined by

$$\dot{\xi}_{i+1} = \dot{\xi}_i + \alpha_1 \ddot{\xi}_i \Delta t \quad \xi_{i+1} = \xi_i + \dot{\xi}_i \Delta t + \alpha_2 \ddot{\xi}_i \Delta t^2 \tag{20}$$

where ξ is the general coordinate of either u or η, and the tuning parameters are

$$\alpha_1 = \alpha_2 = \frac{4[\tilde{M}]}{4[\tilde{M}] + 2[\tilde{C}]\Delta t + [\tilde{K}]\Delta t^2} \tag{21}$$

The matrices with a "tilde" are the general mass, damping, and stiffness matrices from either Eq. (3) or Eq. (18).

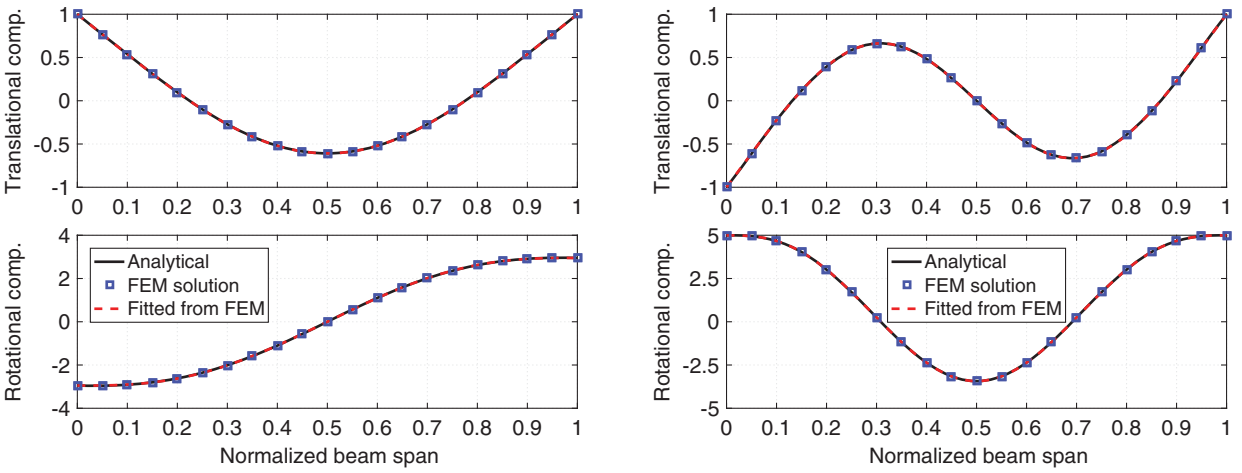

a) First symmetric bending mode

b) First antisymmetric bending mode

Fig. 9 Free–free bending mode shapes from analytical and finite element (20 elements) solutions and the fitted continuous shape (using 20 shifted Legendre polynomials).

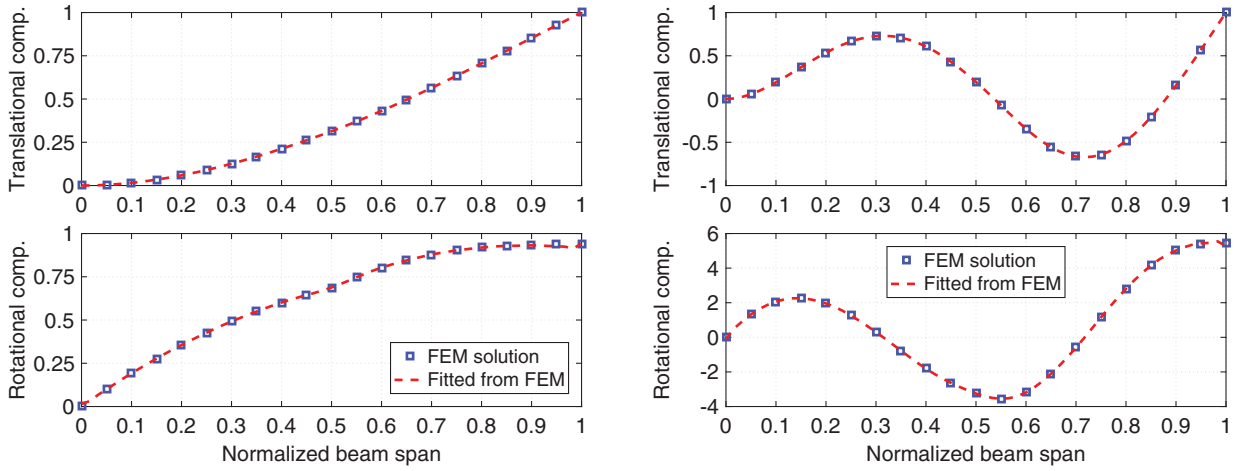

a) First bending mode

b) Third bending mode

Fig. 10 Cantilever nonuniform beam bending mode shapes from finite element (20 elements) solution and the fitted shape (using 20 shifted Legendre polynomials).

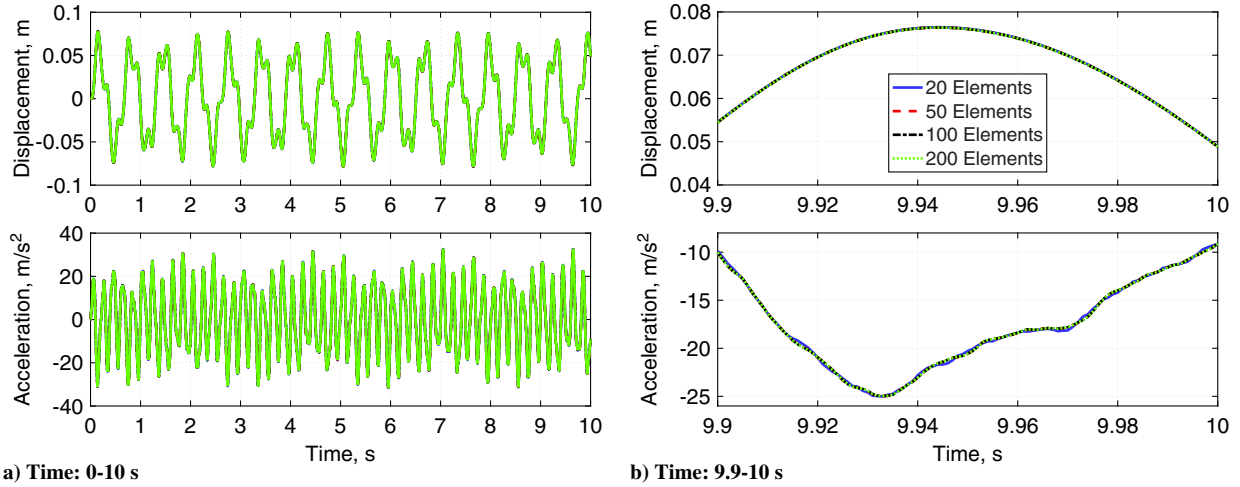

a) Time: 0-10 s

b) Time: 9.9-10 s

Fig. 11 Beam tip displacement and translational acceleration from direct integrations of finite element models.

Table 3 CPU time vs. complexity of beam models

Model	20 elements	50 elements	100 elements	200 elements	6 modes from 200 elements
Dimension of problem	40	100	200	400	20
Total CPU time, s	1.48	11.81	36.41	165.06	1.56
Average CPU time per step, s	1.48×10^{-3}	1.18×10^{-2}	3.64×10^{-2}	1.65×10^{-1}	1.56×10^{-3}

F. Indirect Solution

As discussed, the instantaneous lateral loads acting on the flexible rocket may be unknown in an individual launch because of the random gust. However, limited sensor measurements of the strain and kinematic quantities are available. This capability to find the beam dynamic solution under such a condition is particularly important in the real-time control of launch vehicles. In this case, the direct integration of the equation of motion [Eq. (3) or Eq. (18)] is not feasible. Instead, an indirect solution of the modal magnitude $\eta(t)$ can be obtained based on the available strain measurements $\varepsilon_x(x,t)$ from the FOS along the beam, subject to the constraints of the inertial measurements $[\omega_z(s,t)$ and $a_y(s,t)]$ from the IMU at a single location of $x = s$.

1. *Strain from FOS*

If $\varepsilon_x(x,t)$ is measured by the FOS, the instantaneous modal magnitudes $\eta(t)$ are solved from the first equation of Eq. (15):

$$[B_1]\{\eta\} = \{D_1\} \tag{22}$$

where

$$[B_1] = -z_0[P'']\![A] \quad \{D_1\} = \varepsilon_x(x,t) \tag{23}$$

It can be seen that B_1 contains the system's modal information and D_1 consists of the instantaneous measurement by the FOS.

2. *Angular Velocity from IMU*

If $\omega_y(s,t)$ is measured by the IMU at $x = s$, the instantaneous modal magnitudes $\eta(t)$ should satisfy the following relation derived from Eq. (15):

$$\{\bar{B}_2\}\{\dot{\eta}(t)\} = \bar{D}_2 \tag{24}$$

where

$$\{\bar{B}_2\} = \{P'(s)\}[A] \quad \bar{D}_2 = \omega_y(s,t) \tag{25}$$

A backward finite difference is used to find the rate of the modal magnitude, i.e.,

$$\dot{\eta}(t) = \dot{\eta}_t = \frac{\eta_t - \eta_{t-\Delta t}}{\Delta t} \tag{26}$$

where the step of Δt is determined by the sampling frequency of the IMU. Substituting Eq. (26) in Eq. (24) yields

$$\{B_2\}\{\eta(t)\} = D_2 \tag{27}$$

where

$$\{B_2\} = \{\bar{B}_2\} \quad D_2 = \bar{D}_2\Delta t + \{\bar{B}_2\}\{\eta_{t-\Delta t}\} \tag{28}$$

Obviously, it requires knowing the history of the solution in order to solve the magnitude $\eta(t)$.

3. *Translational Acceleration from IMU*

If $a_z(s,t)$ is measured by the IMU at $x = s$, the instantaneous modal magnitudes $\eta(t)$ should also satisfy the following relation derived from Eq. (15):

$$\{\bar{B}_3\}\{\ddot{\eta}(t)\} = \bar{D}_3 \tag{29}$$

where

$$\{\bar{B}_3\} = \{P(s)\}[A] \quad \bar{D}_3 = a_z(s,t) \tag{30}$$

The approximation of the acceleration of η using the backward finite difference scheme is

$$\ddot{\eta}_t = \frac{\eta_t - 2\eta_{t-\Delta t} + \eta_{t-2\Delta t}}{\Delta t^2} \tag{31}$$

Equations (29) and (31) result in

$$\{B_3\}\{\eta(t)\} = D_3 \tag{32}$$

where

$$\{B_3\} = \{\bar{B}_3\} \quad D_3 = \bar{D}_3\Delta t^2 + \{\bar{B}_3\}\{2\eta_{t-\Delta t} - \eta_{t-2\Delta t}\} \tag{33}$$

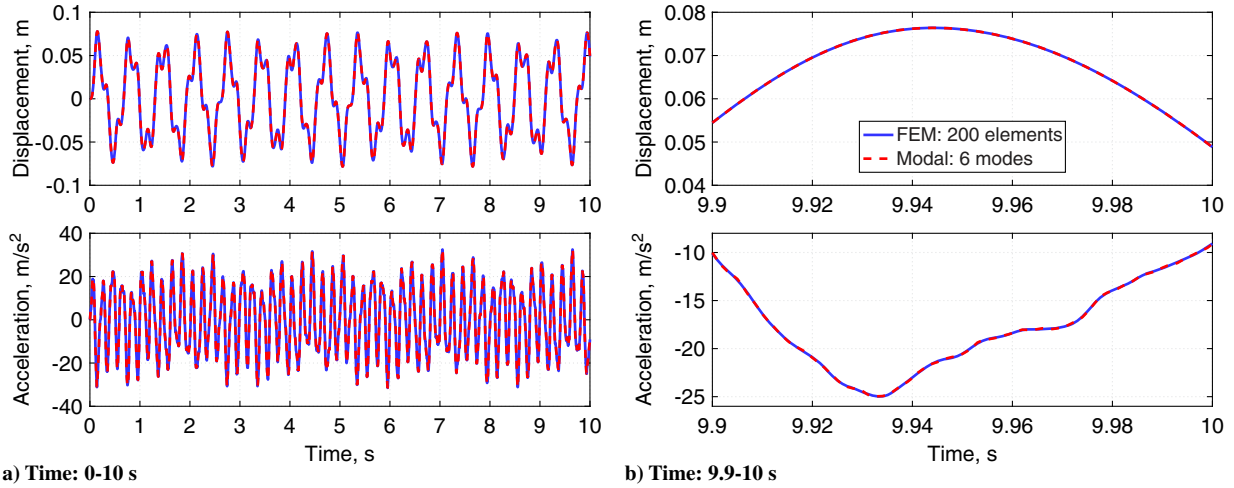

a) Time: 0-10 s b) Time: 9.9-10 s

Fig. 12 Beam tip displacement and translational acceleration from finite element and modal solutions.

4. Combined Solution

One can solve for the current modal magnitude $\eta(t)$ that satisfies the measurements of both the FOS and IMU by combining Eqs. (23), (27), and (32), which is

$$\{\eta\} = [B]^{-1}\{D\} \tag{34}$$

where

$$[B]^T = [\,B_1^T \quad B_2^T \quad B_3^T\,] \quad \{D\}^T = \{\,D_1^T \quad D_2^T \quad D_3^T\,\} \tag{35}$$

In practice, a pseudoinverse of the $[B]$ matrix is required because it is generally not invertible.

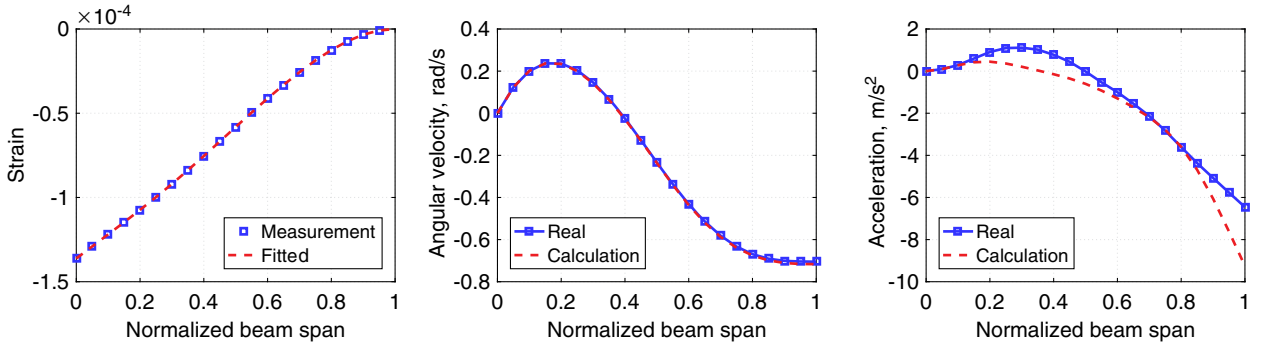

Fig. 13 Fitted strain, estimated velocity, and acceleration using 20-element FEM simulation data.

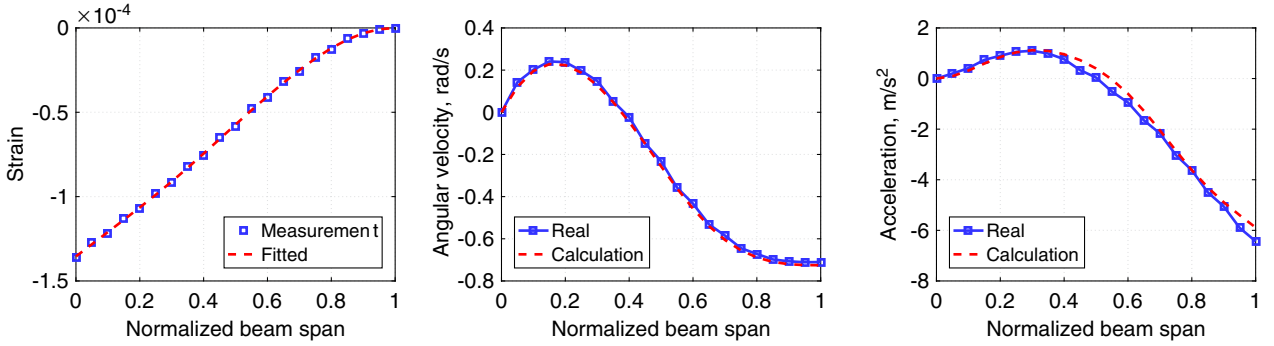

Fig. 14 Fitted strain, estimated velocity, and acceleration using 50-element FEM simulation data.

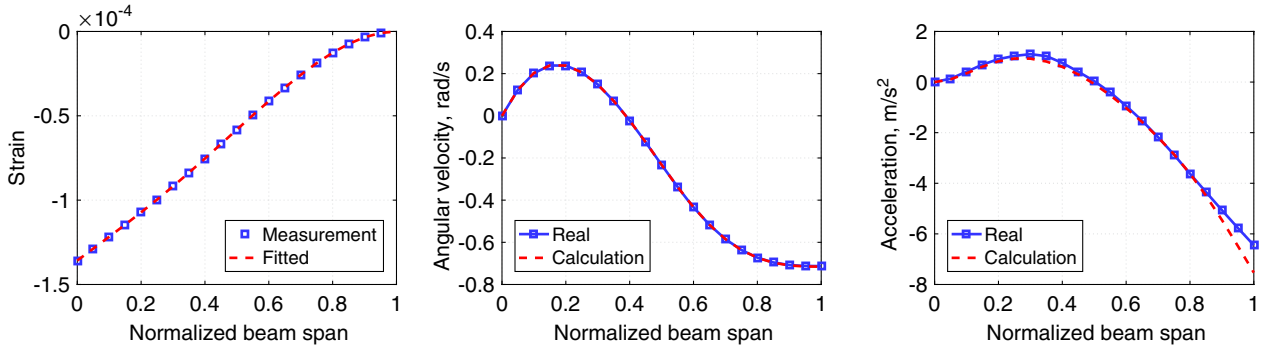

Fig. 15 Fitted strain, estimated velocity, and acceleration using 100-element FEM simulation data.

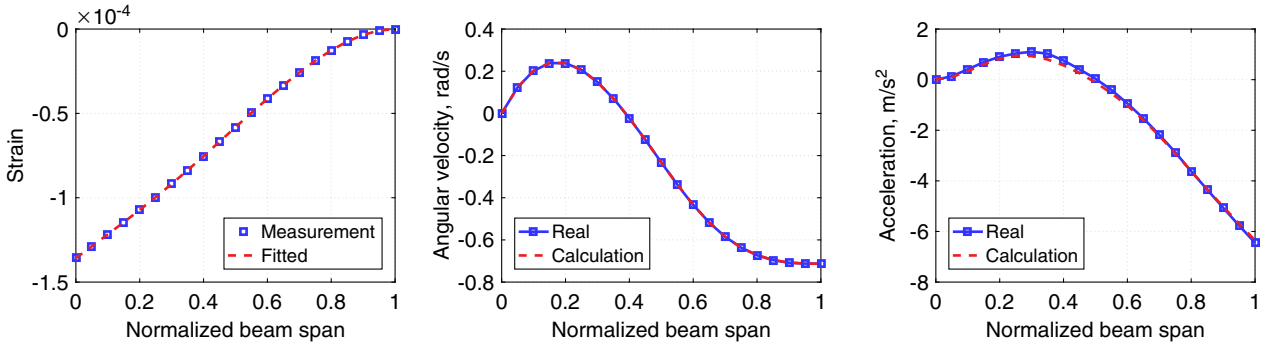

Fig. 16 Fitted strain, estimated velocity, and acceleration using 200-element FEM simulation data.

5. Estimation of Spanwise Angular Velocity and Translational Acceleration

In the last step, one needs to estimate the angular velocity and translational acceleration along the beam reference line based on the solution of η and the kinematics. From Eq. (15), the spanwise angular velocity and translational acceleration are

$$\omega_y(x,t) = [P'(x)][A]\{\dot{\eta}(t)\} = \frac{1}{\Delta t}[P'(x)][A]\{\eta_t - \eta_{t-\Delta t}\}$$
$$a_z(x,t) = [P(x)][A]\{\ddot{\eta}(t)\} = \frac{1}{\Delta t^2}[P(x)][A]\{\eta_t - 2\eta_{t-\Delta t} + \eta_{t-2\Delta t}\} \tag{36}$$

As can be seen from Eqs. (34) and (36), the indirect solution of the beam dynamics involves main operation of linear algebra and matrix operations. The $[B]$ matrix can be fully prearranged if the structural model is known. One only has to update the $\{D\}$ vector based on the sampling data of the IMU and FOS. Therefore, the total computational cost is very low, which does satisfy the "real-time" requirement.

III. Numerical Studies

Both the direct and indirect real-time solutions of a representative beam model are presented in this section. Accuracy of the solutions will be discussed based on the simulation data.

A. Approximate Mode Shapes of a Flexible Beam

Geometrical and material properties of a beam model are listed in Table 1. The cross section of the beam is rectangular. The fiber-optical sensors are assumed to be attached on the wider surface. Therefore, the distance of the sensors to the beam reference line in the current study is $z_0 = b/2$.

The natural frequencies and discrete mode shapes of the beam are first calculated using the finite element model, with the mesh being refined. Table 2 and Fig. 5 compare the natural frequencies obtained from these finite element models and the analytical solutions obtained by solving the characteristic equation of the continuous uniform beam. If one needs the relative error of the first five modes (below 100 Hz; see Table 2) to be less than 0.1%, a 14-element mesh of the beam is sufficient. However, the purpose of the finite element model and the eigenvalue solution is to provide the discrete mode shapes to be fitted by the Legendre polynomials. A finer mesh may improve the quality of the fitted mode shapes. For this reason, a 20-element mesh of the beam is used. Once the finite element model is created, the corresponding number of Legendre polynomials should be properly selected. Figure 6 plots the fitted modes of the beam using 26 shifted Legendre polynomials based on the 20-element mesh. Even though most of the data points are well fitted, the root and tip regions exhibit large errors between the fitted modes and those from the finite element model (FEM) solution. This is because the higher-order Legendre polynomials have larger slopes at the two ends. Thus, they need more data points for a proper fit. Figure 7 compares the good fit with 20 Legendre polynomials instead. The analytical solutions of the mode shapes are also plotted to verify the accuracy of the fitted modes.

One more verification is to check the derivatives of the fitted mode shapes. For the cantilever beam, its curvature and slope of the curvature at the free end must be zero. Correspondingly, the second and third derivatives of the translational component of the mode shapes should be zero at the free end, which has been captured by the fitted modes, as seen in Fig. 8.

The shifted Legendre polynomials can also be used to approximate mode shapes of other beam configurations. Figure 9 demonstrates that the mode shapes of a uniform beam with a free–free boundary condition can be correctly fitted. Figure 10 illustrates how accurately the modes of a nonuniform beam are approximated, where the stiffness of the outer half-board of the beam is reduced to the half of the nominal one.

B. Direct Time Integration

In this section, the root acceleration excitation of the beam is assumed to be a sinusoidal function of $a_B = 10\sin(10\pi t)$ m/s^2. No structural damping is included in this simulation. The Chen–Ricles scheme from [22,25] is implemented for the numerical integrations of the beam equations. A first study is to numerically integrate the finite element-based equation [Eq. (3)], where the beam is divided into 20,

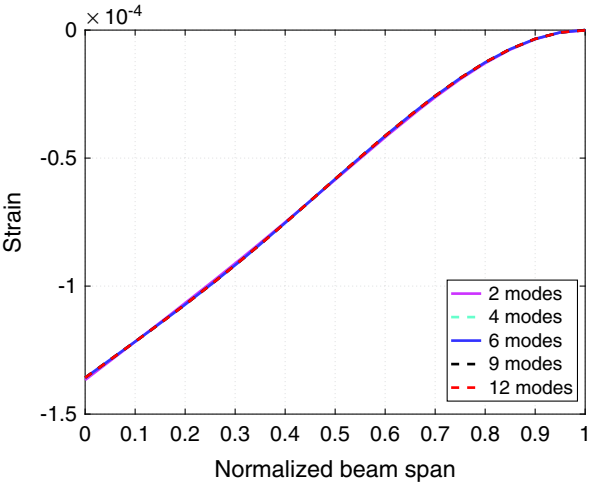

Fig. 17 Fitted strain along the beam using different numbers of modes.

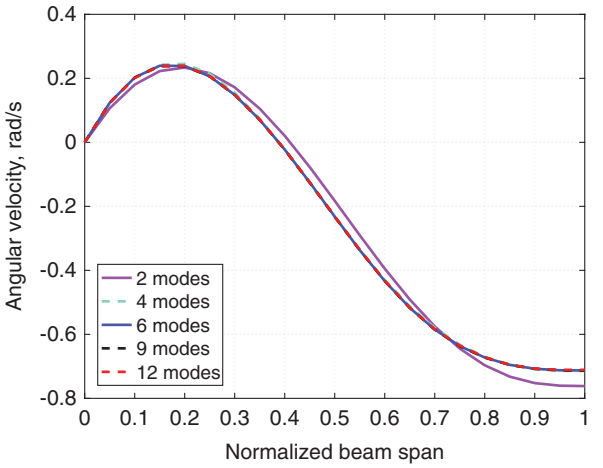

Fig. 18 Estimated angular velocity along the beam using different numbers of modes.

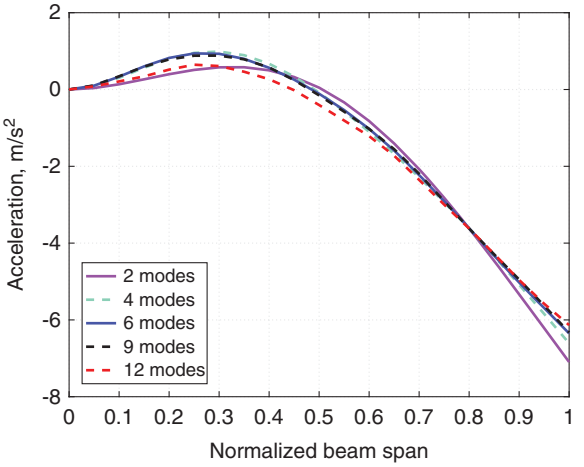

Fig. 19 Estimated translational acceleration along the beam using different numbers of modes.

Table 4 RMS error between recovered and real translational accelerations

Number of modes for approximation	RMS error, m/s^2
1	1.237
2	0.316
3	0.102
4	0.104
5	0.119
6	0.108
7	0.120
8	0.156
9	0.128
10	0.697
11	0.231
12	0.317

50, 100, and 200 elements, respectively. Figure 11 compares the resulting beam tip displacement and translational acceleration in the lateral direction using these models of different meshes. Note that the sampling frequencies of the FOS and IMU are 1000z and 100 Hz, respectively, whereas the onboard autopilot system operates at a lower frequency of 50 Hz. So, the maximum time step to match the autopilot system is 0.02 s for the numerical simulations. In all simulations of the current study, the time step is set to 0.01 s to accommodate any additional delay due to data processing. Further smaller time steps will obviously increase the difficulty of implementing the simulations in the real time. Table 3 lists the total CPU time cost of the entire 10 s simulation and the average CPU time of one step of each solution with different meshes. Overall, all the solutions provide very close results of displacement. They may show some discrepancies in the acceleration results from Fig. 11. As the translational acceleration will be an important quantity to be used for the real-time control development, it is desired to use a finer mesh to reach a more accurate solution of the acceleration. However, the finite element solution using 200 elements, which is believed to be the closest to the true solution, is far from satisfying the requirement of the real-time solutions. In fact, only the 20-element model can allow for the simulation at the real-time rate (i.e., to finish one time step within 0.01 s), as observed from Table 3. However, its solution accuracy may not be satisfactory.

To resolve this issue, a modal-based transient solution is used. Here, the first six modes of the 200-element finite element model are represented by 20 shifted Legendre polynomials. Note that the sixth mode is already above the sensitivity range of the autopilot system. The resulting modal-based equation is still integrated using the Chen–Ricles scheme. The same time step is used. The CPU time of the simulation is also listed in the last column of Table 3. The beam tip displacement and translational acceleration are compared with those from the 200-element finite element solution (see Fig. 12). The rms errors of the tip displacement and translational acceleration between the modal-based solution and the finite element solution using 200 elements are only 7.28×10^{-7} m and 5.22×10^{-2} m/s^2, respectively. From the results, it can be seen that the solution accuracy is well represented by the modal-based solution using the Chen–Ricles scheme and the corresponding CPU time is reduced to allow for real-time studies.

C. Indirect Solution

The indirect solution of the beam dynamics is described in this section. In the indirect solution, the excitation (particularly the aerodynamic loads) to the beam is unknown. However, intermittent strains along the beam span and a single-point angular velocity and translational acceleration are measured by devices of the FOS and IMU. The target is to estimate the angular velocity and translational acceleration along the whole beam span.

In the current study, the transient response from the direct solution is used as the "measurement" data, even though the input of the indirect solution should be real measurement data from the sensors during flight. Specifically, the IMU measurements are assumed to be the angular velocity and translational acceleration data taken at the 80% span from the beam root. Strains are also extracted from the time simulation data at evenly distributed stations along the beam, coincident with the nodes of the finite element models. The spanwise angular velocity and translational acceleration are also going to be recovered at these points.

The first calculation is based on the transient results of the 20-element finite element model. The first 20 shifted Legendre polynomials are used to approximate the first six modes. Then, the aforementioned approach is used to recover the angular velocity and translational acceleration along the beam. Figure 13 compares the measured and fitted strains, as well as the "real" angular velocity and translational acceleration that are actually extracted from the transient simulation and the calculated data, all at $t = 4$ s. Then, the same calculations are repeated using the 50-, 100-, and 200-element models, respectively. The results are all plotted in Figs. 14–16. From the results shown in Figs. 13–16, one can see that the simulation data from the 20-element finite element model are sufficient to fit the strain and estimate the angular velocity. However, the estimated translational acceleration is still very off. One has to use the transient data from the refined finite element model in order to accurately estimate the translational acceleration, as shown in Fig. 16.

It is important to understand the impact of the number of modes on the solution's accuracy. The transient response from the 200-elelment finite element model is used as the measurement, and different numbers of modes are used to represent the beam deformation. Five different cases involving 2, 4, 6, 9, and 12 modes, respectively, are studied. All modes are then approximated by 20 shifted Legendre polynomials. Figures 17–19 compare the fitted strains and estimated

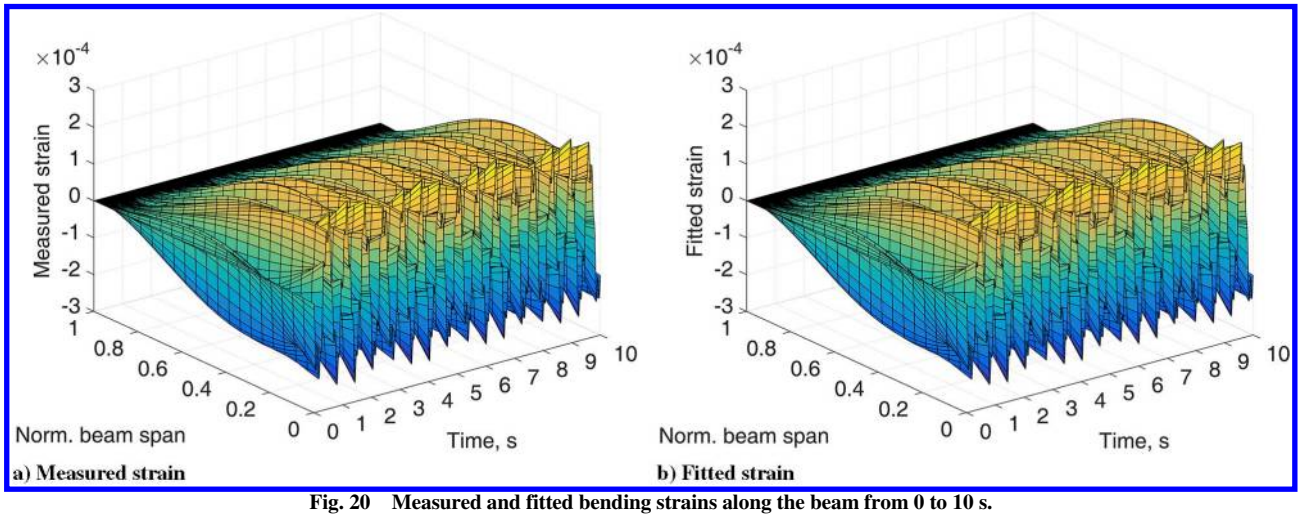

Fig. 20 Measured and fitted bending strains along the beam from 0 to 10 s.

angular velocities and translational accelerations. It is not a surprise that the two-mode representation of the beam deformation is almost sufficient to fit the strain (Fig. 17). However, accurate estimations of the velocity and acceleration along the beam need more modes (Figs. 18 and 19). Additionally, the inclusion of excessive modes may also compromise the solution of acceleration, which is highlighted by the result with 12 modes. Table 4 also shows such a trend. In fact, there needs to be more shifted Legendre polynomials to accurately approximate the higher-order mode shapes [see Eq. (12)]. A fixed number of 20 shifted Legendre polynomials may not be sufficient for the higher-order mode involved in the table. On the other hand, because the autopilot system works at 50 Hz, it is not sensitive to the higher-order modes anyway. Therefore, involving more higher-order modes and using more shifted Legendre polynomials are unnecessary. In the current study, the first six modes are retained in the modal solution.

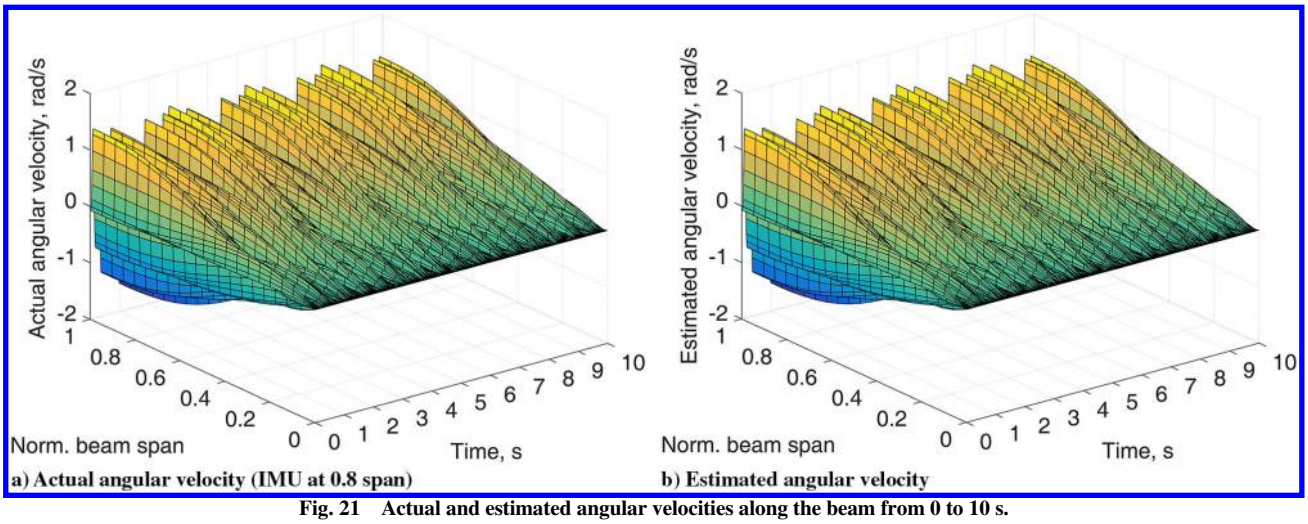

a) Actual angular velocity (IMU at 0.8 span) b) Estimated angular velocity

Fig. 21 Actual and estimated angular velocities along the beam from 0 to 10 s.

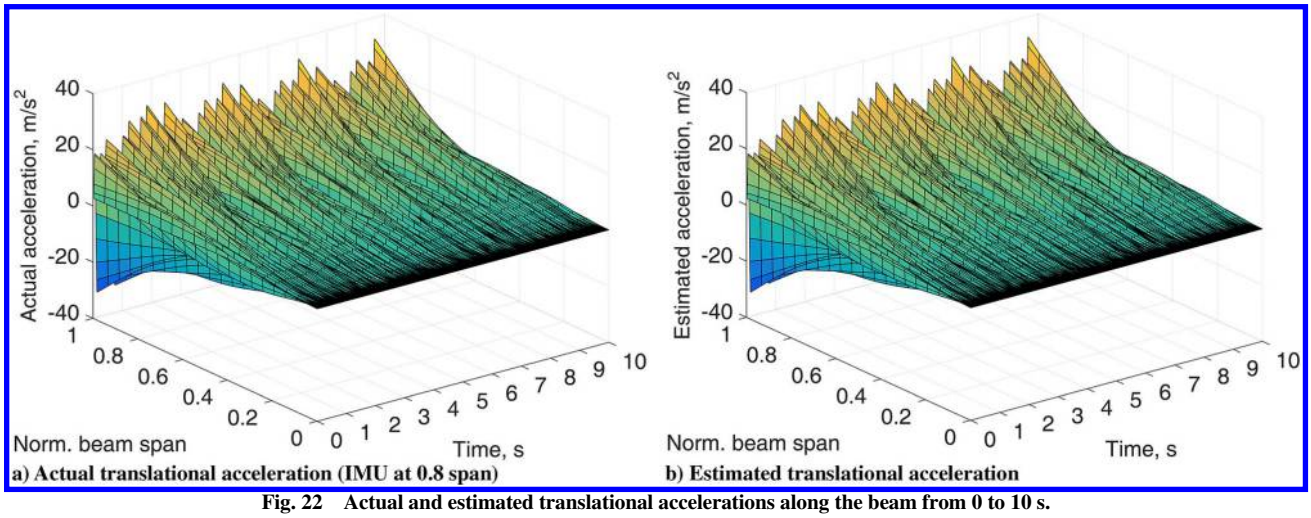

a) Actual translational acceleration (IMU at 0.8 span) b) Estimated translational acceleration

Fig. 22 Actual and estimated translational accelerations along the beam from 0 to 10 s.

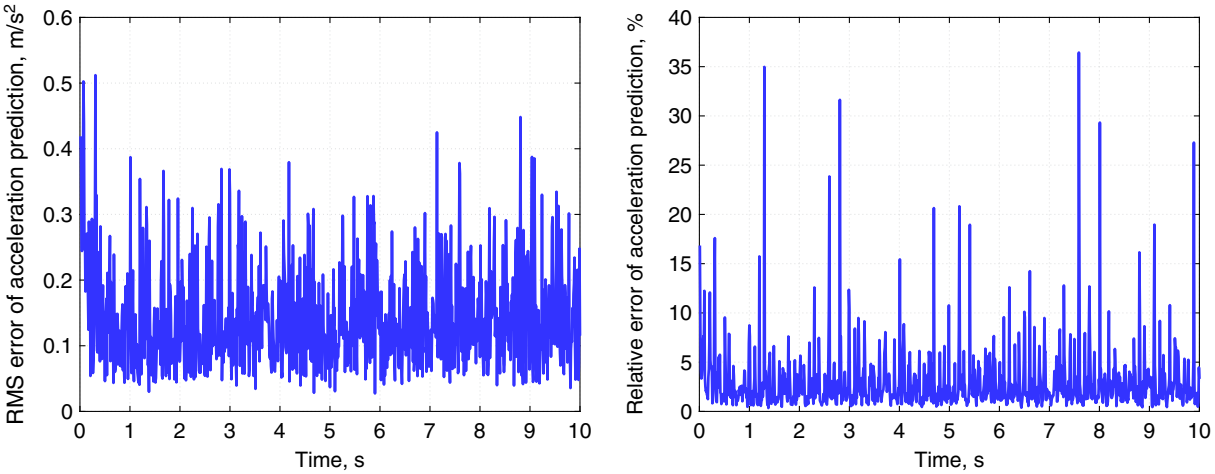

a) Absolute rms error b) Relative error compared to average acceleration

Fig. 23 Absolute and relative errors of estimated translational acceleration without structural damping.

For the indirect solution performed so far, it is all at $t = 4$ s. The solution process is repeated in the time range of 0 to 10 s. Data from the direct time integration, including the bending strain along the beam (as the FOS measurements) as well as the angular velocity and translational acceleration at the 80% beam span (as the IMU measurements) are extracted and serve as the input to the indirect solution. Figures 20–22 compare the spanwise bending strain, angular velocity, and translational acceleration between the indirect solution and the measurement or "actual" data (essentially, results from the direct time integration). Because the prediction error of spanwise acceleration is usually higher than that of the velocity, due to the second-order finite difference used in Eq. (31), its accuracy is studied here. At a given time, the relative error of the acceleration estimation is defined as

$$e_a(t) = \frac{a_{\text{err}}(t)}{\bar{a}(t)} \tag{37}$$

where

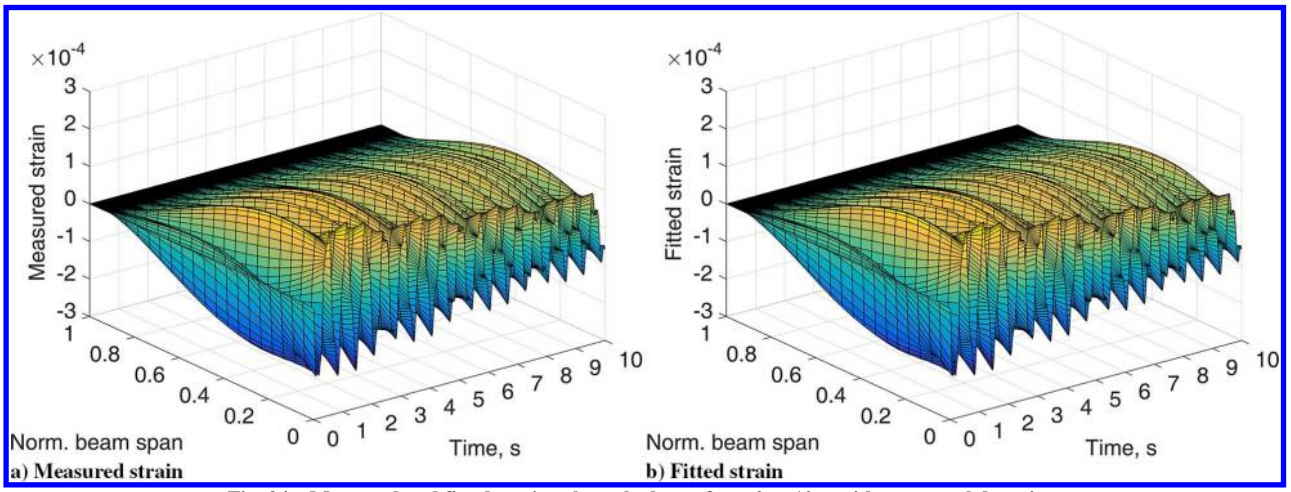

Fig. 24 Measured and fitted strains along the beam from 0 to 10 s, with structural damping.

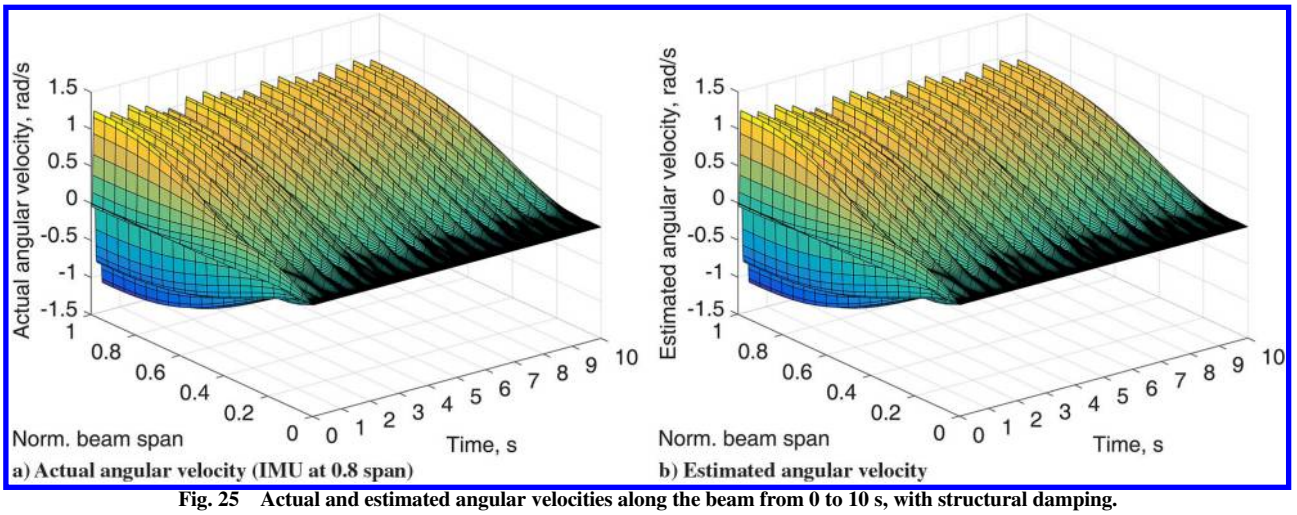

Fig. 25 Actual and estimated angular velocities along the beam from 0 to 10 s, with structural damping.

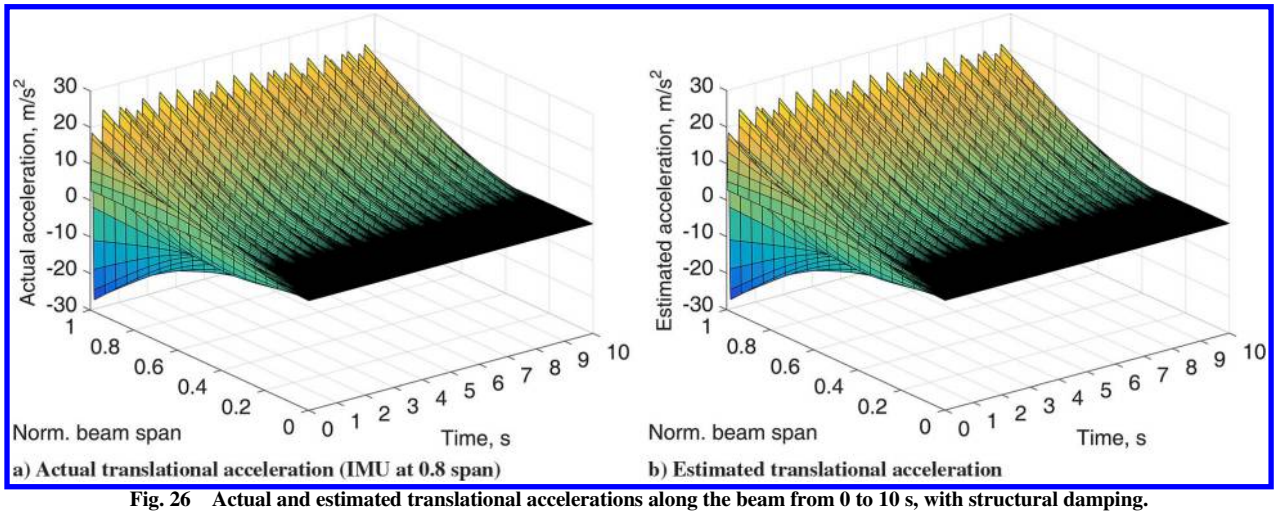

Fig. 26 Actual and estimated translational accelerations along the beam from 0 to 10 s, with structural damping.

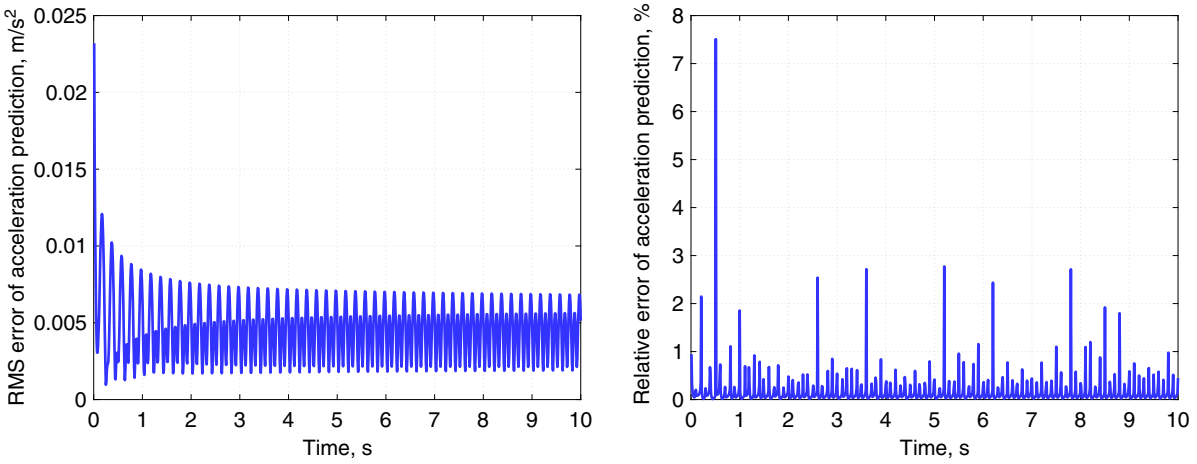

a) Absolute rms error **b) Relative error compared to average acceleration**

Fig. 27 Absolute and relative errors of estimated translational acceleration with structural damping.

$$a_{\text{err}}(t) = \sqrt{\frac{1}{N_{x_i}}\sum_{x_i}[a_{z1}(x_i,t) - a_{z2}(x_i,t)]^2}$$

$$\bar{a}(t) = \sqrt{\frac{1}{N_{x_i}}\sum_{x_i}a_{z2}(x_i,t)^2} \tag{38}$$

where x_i are all locations of the FOSs, a_{z1} are the spanwise accelerations estimated from Eq. (36), and a_{z2} are the real spanwise accelerations of the beam at time t. Again, they are essentially results from the direct time integration. Based on the equations, the time histories of the absolute and relative errors (a_{err} and e_a, respectively) are plotted in Fig. 23. Generally, the relative error of the acceleration estimation is low, with singular points when the average acceleration $\bar{a}$ is close to zero. From the results, it is evident that the accuracy of the indirect solution is well maintained throughout the time range.

Finally, damping is considered for the beam, where the stiffness-proportional damping coefficient α is assumed to be 0.002. The modal-based transient simulation of the damped system is performed, such that the bending strain along the beam (as the FOS measurements) as well as the angular velocity and translational acceleration at the 80% beam span (as the IMU measurements) are extracted and serve as the input to the indirect solution. The indirect solution is also repeated in the time range of 0 to 10 s. Figures 24–26 compare the spanwise bending strain, angular velocity, and translational acceleration between the indirect solution and the measurement or actual data (essentially, results from the direct time integration). Figure 27 plots the time histories of the estimation errors of the translational acceleration. From the side-to-side comparisons, one can see the indirect solution approach is also applicable to damped systems, even though the damping was not considered in the original development of the indirect solution process.

IV. Conclusions

Based on Euler–Bernoulli beam theory, analytical and numerical approaches were derived and implemented in this paper for real-time solutions of the bending dynamics of flexible rockets. The finite element discretization of the beam model was used at the beginning, where the discrete mode shapes were extracted and represented by using continuous shifted Legendre polynomials. This treatment allowed for the spatial derivatives of the finite element model's discrete mode shapes in order to represent the rotation and curvature as continuous functions.

By implementing an explicit Newmark-based scheme, the direct time integration of the beam bending equation could be finished in the real-time rate. In real-time control operations of flexible rockets, the external excitation to the vehicle may not be known. To enable control of flexible rockets in real-time, an indirect solution of beam bending dynamics was also explored in the paper, where only limited beam bending strains and kinematic quantities were measured. To find the distributed bending dynamics along the beam, the modal magnitude of the beam was solved by taking advantage of the approximation of the modes using the shifted Legendre polynomials, subject to the available sensor measurements. A backward finite difference was used to calculate the rate and acceleration of the modal magnitudes. This study successfully established a quick, non-iterative, analytical solution of the beam dynamics, based on the available sensor measurements. Each of the indirect solutions could be finished in about 10^{-3} s, which satisfied the requirement of further real-time control developments, as this was much faster than the sampling rates of an onboard FOS, IMU, and autopilot system. The solution was accurate and stable for perfect measurement data because the spanwise angular velocity and translational acceleration were both precisely estimated. The derived formulations were capable of handling 1) nonuniform beam stiffness, 2) nonuniform inertia distribution, 3) different IMU locations, 4) various boundary conditions, and 5) potential two- or three-degree-of-freedom beam bending and torsion.

Acknowledgments

This work was supported by the NASA Launch Services Program Special Study LSP-14-015. The second author acknowledges the support of the Graduate Council Fellowship from the University of Alabama. Technical discussions on the numerical integration scheme with Wei Song (Civil Engineering, University of Alabama) are gratefully acknowledged. The views expressed in this paper are those of the authors and do not reflect the official policy or position of NASA or the U.S. Government.

References

[1] Leitmann, G., "On the Equation of Rocket Motion," *Journal of the British Interplanetary Society*, Vol. 16, 1957, pp. 141–147.

[2] Stengel, R. F., "Flight Performance of a Small, Low-Altitude Rocket," *Journal of Spacecraft and Rockets*, Vol. 3, No. 6, 1966, pp. 938–939. doi:10.2514/3.28569

[3] Vinh, N. X., "General Theory of Optimal Trajectory for Rocket Flight in a Resisting Medium," *Journal of Optimization Theory and Applications*, Vol. 11, No. 2, 1973, pp. 189–202. doi:10.1007/BF00935883

[4] Eke, F. O., and Cervantes, E., "Dynamics of Axisymmetric Rockets in Free Flight," *Journal of Dynamic Systems Measurement and Control*, Vol. 120, No. 3, 1998, pp. 410–414. doi:10.1115/1.2805418

[5] Lee, B. S., Choi, J. H., and Kwon, O. J., "Numerical Simulation of Free-Flight Rockets Air-Launched from a Helicopter," *Journal of Aircraft*, Vol. 48, No. 5, 2011, pp. 1766–1775. doi:10.2514/1.C031365

[6] Anderson, J. D., *Introduction to Flight*, 3rd ed., McGraw–Hill Series in Aeronautical and Aerospace Engineering, McGraw–Hill, New York, 1989.

[7] Reis, G. E., and Sundberg, W. D., "Calculated Aeroelastic Bending of a Sounding Rocket Based on Flight Data," *Journal of Spacecraft and Rockets*, Vol. 4, No. 11, 1967, pp. 1489–1494. doi:10.2514/3.29118

[8] Choi, H. D., and Bang, H., "An Adaptive Control Approach to the Attitude Control of a Flexible Rocket," *Control Engineering Practice*, Vol. 8, No. 9, 2000, pp. 1003–1010. doi:10.1016/S0967-0661(00)00032-0

[9] Huang, X., and Zeiler, T. A., "Dynamics of Flexible Launch Vehicles with Variable Mass," *44th AIAA Aerospace Sciences Meeting and Exhibit*, AIAA Paper 2006-0826, Jan. 2006.

[10] Hu, P., and Ren, G., "Multibody Dynamics of Flexible Liquid Rockets with Depleting Propellant," *Journal of Guidance, Control, and Dynamics*, Vol. 36, No. 6, 2013, pp. 1849–1855. doi:10.2514/1.59848

[11] Crimi, P., "Aeroelastic Stability and Response of Flexible Tactical Weapons," *22nd AIAA Aerospace Sciences Meeting*, AIAA Paper 1984-0392, Jan. 1984.

[12] Chae, S., and Hodges, D. H., "Dynamics and Aeroelastic Analysis of Missiles," *44th AIAA/ASME/ASCE/AHS/ASC Structures, Structural Dynamics, and Materials Conference*, AIAA Paper 2003-1968, April 2003.

[13] Hodges, D. H., "A New Approach to Aeroelastic Response, Stability and Loads of Missiles and Projectiles," U.S. Army Project Rept. ADA424568, Nov. 2004.

[14] Allen, H. J., "Estimation of the Forces and Moments Acting on Inclined Bodies of Revolution," NACA TR RM A9I26, Nov. 1949.

[15] Bisplinghoff, R., Ashley, H., and Halfman, R., *Aeroelasticity*, Dover, Mineola, NY, 1996.

[16] Bartels, R., Chwalowski, P., Massey, S. J., Heeg, J., and Minek, R. E., "Computational Aeroelastic Analysis of the Ares I Crew Launch Vehicle During Ascent," *Journal of Spacecraft and Rockets*, Vol. 49, No. 4, 2012, pp. 651–658. doi:10.2514/1.A32127

[17] Li, J., Kapania, R. K., and Spillman, W. B., Jr., "Placement Optimization of Distributed-Sensing Fiber-Optic Sensors Using Genetic Algorithms," *AIAA Journal*, Vol. 46, No. 4, 2008, pp. 824–836. doi:10.2514/1.25090

[18] "Dryden Fiber Optic Sensing Technology Suite," http://www.nasa.gov/offices/ipp/centers/dfrc/technology/Fiber-Optic-Sensing-Suite_prt.htm [retrieved 24 Nov. 2015].

[19] Wolf, M. G., Griffin, E. D., Gutierrez, H., Suhey, J. D., Su, W., and Stanley, J. E., "Flexible Body Control Using Fiber Optic Sensors (FlexFOS)," NASA Technology Transfer System, NASA Rept. 1426097577, 2015.

[20] Gutierrez, H., Javani, B. S., Kirk, D., Su, W., Wolf, M., and Griffin, E., "Fiber Optic Sensor Arrays for Real-Time Virtual Instrumentation and Control of Flexible Structures," *Proceedings of Structural Health Monitoring, Damage Detection & Mechatronics, Volume 7: Proceedings of the 34th IMAC, A Conference and Exposition on Structural Dynamics 2016*, edited by Wicks, A., and Niezrecki, C., Springer International Publ., 2016, pp. 9–22.

[21] Shearer, C. M., and Cesnik, C. E. S., "Modified Generalized-α Method for Integrating Governing Equations of Very Flexible Aircraft," *47th AIAA/ASME/ASCE/AHS/ASC Structures, Structural Dynamics, and Materials Conference*, AIAA Paper 2006-1747, May 2006.

[22] Chen, C., and Ricles, J. M., "Development of Direct Integration Algorithms for Structural Dynamics Using Discrete Control Theory," *Journal of Engineering Mechanics*, Vol. 134, No. 8, 2008, pp. 676–683. doi:10.1061/(ASCE)0733-9399(2008)134:8(676)

[23] Pourtakdoust, S. H., and Assadian, N., "Investigation of Thrust Effect on the Vibrational Characteristics of Flexible Guided Missiles," *Journal of Sound and Vibration*, Vol. 272, Nos. 1–2, 2004, pp. 287–299. doi:10.1016/S0022-460X(03)00779-X

[24] Abramowitz, M., and Stegun, I. A., *Handbook of Mathematical Functions*, Dover, New York, 1968.

[25] Chen, C., and Ricles, J. M., "Stability Analysis of Direct Integration Algorithms Applied to Nonlinear Structural Dynamics," *Journal of Engineering Mechanics*, Vol. 134, No. 9, 2008, pp. 703–711. doi:10.1061/(ASCE)0733-9399(2008)134:9(703)

V. Babuska
Associate Editor